2-10-2017

Nonlinear Ionospheric Responses to Large-Amplitude Infrasonic-Acoustic Waves Generated by Undersea Earthquakes

M. D. Zettergren
Embry-Riddle Aeronautical University, zettergm@erau.edu

J. B. Snively
Embry-Riddle Aeronautical University, snivelyj@erau.edu

A. Komjathy
Jet Propulsion Laboratory, California Institute of Technology

O. P. Verkhoglyadova
Jet Propulsion Laboratory, California Institute of Technology

AGU PUBLICATIONS

JGR

Journal of Geophysical Research: Space Physics

RESEARCH ARTICLE

10.1002/2016JA023159

Key Points:
- Large undersea earthquakes generate large-amplitude acoustic waves with compressional velocities exceeding 200 m/s
- Modeled ionospheric responses to the 2011 Tohoku earthquake, including TEC depletions, are consistent with the data
- TEC depletions are shown to be a result of an initial acoustic shock followed by nonlinear, dissipating acoustic waves in the thermosphere.

Supporting Information:
- Supporting Information S1
- Movie S1
- Movie S2

Correspondence to:
M. D. Zettergren,
zettergm@erau.edu

Citation:
Zettergren, M. D., J. B. Snively, A. Komjathy, and O. P. Verkhoglyadova (2017), Nonlinear ionospheric responses to large-amplitude infrasonic-acoustic waves generated by undersea earthquakes, *J. Geophys. Res. Space Physics*, *122*, 2272–2291, doi:10.1002/2016JA023159.

Received 12 JUL 2016
Accepted 11 JAN 2017
Accepted article online 14 JAN 2017
Published online 10 FEB 2017

Nonlinear ionospheric responses to large-amplitude infrasonic-acoustic waves generated by undersea earthquakes

M. D. Zettergren[1,2], J. B. Snively[1], A. Komjathy[3], and O. P. Verkhoglyadova[3]

[1]Department of Physical Sciences and Center for Space and Atmospheric Research, Embry-Riddle Aeronautical University, Daytona Beach, Florida, USA, [2]Center for Space Physics, Boston University, Boston, Massachusetts, USA, [3]Jet Propulsion Laboratory, California Institute of Technology, Pasadena, California, USA

Abstract Numerical models of ionospheric coupling with the neutral atmosphere are used to investigate perturbations of plasma density, vertically integrated total electron content (TEC), neutral velocity, and neutral temperature associated with large-amplitude acoustic waves generated by the initial ocean surface displacements from strong undersea earthquakes. A simplified source model for the 2011 Tohoku earthquake is constructed from estimates of initial ocean surface responses to approximate the vertical motions over realistic spatial and temporal scales. Resulting TEC perturbations from modeling case studies appear consistent with observational data, reproducing pronounced TEC depletions which are shown to be a consequence of the impacts of nonlinear, dissipating acoustic waves. Thermospheric acoustic compressional velocities are ~±250–300 m/s, superposed with downward flows of similar amplitudes, and temperature perturbations are ~300 K, while the dominant wave periodicity in the thermosphere is ~3–4 min. Results capture acoustic wave processes including reflection, onset of resonance, and nonlinear steepening and dissipation—ultimately leading to the formation of ionospheric TEC depletions "holes"—that are consistent with reported observations. Three additional simulations illustrate the dependence of atmospheric acoustic wave and subsequent ionospheric responses on the surface displacement amplitude, which is varied from the Tohoku case study by factors of 1/100, 1/10, and 2. Collectively, results suggest that TEC depletions may only accompany very-large amplitude thermospheric acoustic waves necessary to induce a nonlinear response, here with saturated compressional velocities ~200–250 m/s generated by sea surface displacements exceeding ~1 m occurring over a 3 min time period.

1. Introduction

Ionospheric total electron content (TEC) fluctuations following large-magnitude undersea earthquakes and resulting tsunamis have been identified in many recent investigations [e.g., *Rolland et al.*, 2011; *Kakinami et al.*, 2012; *Galvan et al.*, 2012]. Earthquakes impact the upper atmosphere first through vertical displacements of the Earth's crust or ocean surfaces producing, as one effect, low-frequency acoustic (periods ~1–4 min far infrasound, hereafter referred to as "infrasound") and gravity waves (periods >5 min). These waves can achieve significant amplitudes during upward propagation, their velocity perturbations growing exponentially through the rarefied upper atmosphere until the onset of dissipation, and are capable of driving detectable ionospheric electron density (TEC) fluctuations [e.g., *Artru et al.*, 2005] and dynamo electrical currents [e.g., *Zettergren and Snively*, 2013].

Earthquake-driven ocean surface displacements also generate tsunamis, which couple significant energy into the atmosphere in the form of gravity waves [*Hines*, 1960]. Tsunami-generated gravity waves have been detected via GPS as fluctuations in total electron content (TEC) following large-magnitude earthquakes like the 2001 Peru earthquake [*Artru et al.*, 2005], the 2004 Sumatran earthquakes [*Rolland et al.*, 2010], and the 2011 Tohoku earthquake [*Galvan et al.*, 2012]. These observations and related modeling efforts [*Occhipinti et al.*, 2006; *Hickey et al.*, 2009] indicate that periodicities of tens of minutes and TEC fluctuations in the range of ±1 TEC unit (TECU) (1 TECU = 10^{16} el m^{-2}) are typical signatures of tsunami-generated gravity waves from very strong earthquakes ($M > 8.0$). Recent ionospheric modeling efforts have addressed additional physical processes like interhemispheric electrodynamic coupling effects on ionosphere responses [*Huba et al.*, 2015]. Newly developed models of tsunami-generated atmospheric wave propagation have focused on effects of

spatial and temporal localization of the tsunami ocean wave packet on gravity wave propagation in the atmosphere [*Vadas et al.*, 2015] and effects of partial reflection on tsunami-generated gravity waves [*Broutman et al.*, 2014].

In contrast to studies focused on tsunami-driven gravity wave responses, we here examine impacts of transient acoustic waves generated first by the atmospheric response to the ocean disturbance that *precedes* the tsunami. Earthquake-generated acoustic waves are readily identifiable in GPS observations as ~0.1–2 TECU, 3–5 mHz, oscillations, which are delayed from the quake occurrence by the sound travel time between the ground and ionosphere. In some extreme cases of earthquakes occurring under the ocean, the onset of acoustic oscillations is concurrent with a persistent, sharp decrease in TEC (4–8 TECU) above the epicenter [*Saito et al.*, 2011; *Kakinami et al.*, 2012; *Astafyeva et al.*, 2013a]. Sustained acoustic oscillations at ~3.7 min period, lasting 30 min to 1 h after the earthquake were also detected in TEC perturbations following the Tohoku earthquake [*Saito et al.*, 2011; *Matsumura et al.*, 2011] and have been attributed to vertical acoustic resonance between the ground and thermosphere.

The existence of large TEC oscillations and long-lived TEC depletions suggest that large amplitude, nonlinear acoustic waves can be generated as a consequence of ocean surface responses following undersea earthquakes of strong magnitude ($M > 8.0$). Prior modeling studies indicate that acoustic waves with compressional velocities ~ 100–200 m/s are generated by earthquakes [e.g., *Shinagawa et al.*, 2007; *Rolland et al.*, 2011]. Measurements from the GOCE satellite after the Tohoku earthquake showed ~ 10% neutral density fluctuations at a distance of ~ 2500 km from the epicenter and at an altitude of 270 km [*Garcia et al.*, 2013]. These measurements were used to infer ~ 100 m/s vertical drifts due to acoustic waves, even at these considerable distances [*Garcia et al.*, 2013, section 3]. Analysis of GRACE (Gravity Recovery and Climate Experiment) neutral density perturbations following the 2011 Tohoku earthquake similarly suggested density variations of several percent [*Yang et al.*, 2014]. *Zettergren and Snively* [2015] simulated the response of the ionosphere to acoustic waves from a directive ground-level source and demonstrated the concurrence of ~100–200 m/s plasma drifts with ~0.6 peak-to-peak TEC oscillations for geophysically plausible source scales and amplitudes. It was noted in that study that the simulated TEC perturbations were significantly smaller than those observed during the Tohoku earthquake and, further, that their simulation did not reproduce the strong (~4–8 TECU) depletion observed following the 2011 Tohoku earthquake. Hence, the acoustic wave amplitudes simulated by *Zettergren and Snively* [2015] appear significantly *lower* than those present in the Tohoku event. Further evidence supporting this idea is the simulation study by *Shinagawa et al.* [2013], which suggested that steep, earthquake-generated acoustic waves in the thermosphere are capable of depleting the ionosphere, above the epicenter, by ~5–10 TECU. Theoretical investigations by *Wei et al.* [2015] also agree that transient formation of tsunamis may generate acoustic wave precursors at sufficient amplitudes to steepen into shocks at lower thermospheric altitudes.

In order to fully apply modeling results to interpretation of TEC data, it remains necessary to understand the parameter space of source amplitudes and the resulting ionospheric responses. To date, there has not been a definitive determination of the thermospheric acoustic wave amplitudes during severe earthquake events such as the 2011 Tohoku earthquake. Models of atmospheric-ionospheric response, summarized above, suggest values of at least several hundreds of m/s [*Zettergren and Snively*, 2015], perhaps more [*Shinagawa et al.*, 2013]. However, studies of acoustic responses have not yet (1) calibrated the atmosphere-ionosphere model source amplitudes by using available ocean surface models and data, ionospheric TEC data, and ground-based microbarograph data nor (2) included comprehensive multifluid descriptions of nonlinear dynamics and ionospheric transport, chemistry, and electrodynamics. Within a calibrated, comprehensive modeling suite, the presence of acoustic resonance between the ground and thermosphere [e.g., *Matsumura et al.*, 2011], TEC detectability thresholds for earthquakes of various magnitude [e.g., *Perevalova et al.*, 2014], and impacts of acoustic wave nonlinearity (steepening and dissipation) [e.g., *Shinagawa et al.*, 2013], can be investigated simultaneously and constrained by direct comparisons with observations.

This paper reports a detailed investigation of the ionospheric responses to earthquake-generated acoustic waves using a recently developed, atmosphere-ionosphere modeling suite [*Zettergren and Snively*, 2015]. The purpose of this study is to outline the effects of acoustic wave amplitude and nonlinearity on ionospheric responses, including production of detectable primary and secondary TEC oscillations, semipermanent TEC depletions, and reflections that may lead to subsequent resonances. A simulation case study for the 2011

Tohoku earthquake ($M = 9.0$) is constructed, using published ocean surface modeling and data [*Tsushima et al.*, 2011; *Maeda et al.*, 2011; *Kakinami et al.*, 2012; *Mikumo et al.*, 2013] to guide specification of a simplified source of acoustic waves in the model. This source represents the initial ocean surface displacement following the earthquake (which is responsible for most of the acoustic waves) and does not include the tsunami response of the ocean. The output from our simulations is shown to be consistent with the main features of TEC observations, thus further justifying our source amplitude and timescale and model physics. Results provide quantitative insight into possible acoustic wave amplitudes during the Tohoku earthquake and enable detailed investigations of structured *F* region density layers, density cavities near epicenter, and the properties of infrasonic waves (here with very low frequencies ~ 4.2 – 5.6 mHz and long periods ~3 – 4 min) associated with this event.

Additional simulation case studies are constructed by varying the source amplitude, to simulate the dependence of atmospheric-ionospheric responses of interest (infrasonic wave amplitudes and resulting TEC depletions) for a range of vertical perturbations at the lower boundary of the model. This extends and complements results of *Zettergren and Snively* [2015], which investigated the effects of wave source scales and locations on ionospheric responses. We here focus on the dependence of atmospheric-ionospheric responses on wave amplitude, the role of acoustic wave nonlinearity in determining the character of the ionospheric response, and the utility of TEC information for inferring infrasonic wave amplitudes in the thermosphere.

This paper is organized so that, after our model is introduced, the observable outputs are first examined and compared against available data. Following these validation comparisons, we examine some unobservable details of the ionospheric response and present an analysis of the underlying thermospheric dynamics. Section 2 describes our model and the simulation setup for the 2011 Tohoku earthquake case study. Section 3 presents observables, i.e., TEC perturbations, from the model and compares them against available information from the literature and comprehensive TEC data collected following the 2011 Tohoku earthquake. The distributed ionospheric and thermospheric responses to the 2011 Tohoku earthquake are also examined in this section. Section 4 reports our investigation of the amplitude dependence of the ionospheric and thermospheric responses to ocean surface forcing. Finally, section 5 summarizes results and conclusions.

2. Coupled Atmosphere-Ionosphere Model

The model of neutral atmosphere-ionosphere coupling used in this study is based on an existing model of the atmospheric dynamics [*Snively and Pasko*, 2008; *Snively*, 2013] that has been coupled to an ionospheric model [*Zettergren and Semeter*, 2012], as described in *Zettergren and Snively* [2015, Appendix A]. The atmospheric dynamics model solves the compressible and nonlinear Navier-Stokes system of equations in conservative form (for density, momentum, and energy) using the shock-capturing finite volume method of *LeVeque* [2002], in flux-differencing "*f*-wave" form [*Bale et al.*, 2002]. It is implemented in a modified version of Clawpack 4.3 (http://depts.washington.edu/clawpack/clawpack-4.3/). It here incorporates generation of acoustic waves through an imposed velocity at its sea-level lower boundary. The ionospheric model solves a fluid system of equations for each major ionospheric species and includes an electrostatic description of dynamo currents. This model includes chemical and collisional processes relevant to the *E* and *F* region ionospheres [*Zettergren and Semeter*, 2012, and references therein]. It also computes full time-dependent, nonlinear solutions for ion momentum parallel to the geomagnetic field and ion and electron energy, including the effects of heat fluxes. Coupling between the two models is achieved by passing atmospheric density, velocity, and temperature perturbations into the ionospheric simulation. These perturbations then drive the ionospheric state through chemistry, collisional heating and cooling, drag, and through the production of dynamo electric fields. Our model enables direct computation of observable quantities, such as vertical TEC and magnetic field fluctuations due to infrasound-dynamo ionospheric currents.

The atmospheric dynamics model uses a two-dimensional, cylindrical, axisymmetric grid and is appropriate for sources that are localized or circular/spherical in nature [*Snively*, 2013]. This grid covers a radial distance of $0 \leq r \leq 750$ km (a total horizontal distance of 1500 km) and an altitude range of $0 \leq z \leq 750$ km. The ionospheric model uses a two-dimensional dipole curvilinear mesh [e.g., *Huba et al.*, 2000] to encapsulate interhemispheric mapping of electric fields and currents from neutral wave sources [e.g., *Zettergren and Snively*, 2013, 2015; *Huba et al.*, 2015]. The particular mesh used in this study covers the ionosphere from altitudes ranging from ~80 to 3700 km. The center latitude and longitude of both the neutral and ionosphere

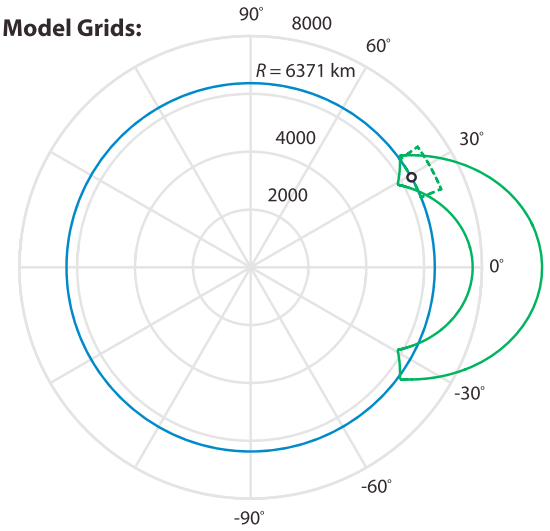

Figure 1. Atmospheric-ionospheric dynamics model grids used in this study. The green dashed lines mark the edges of the atmospheric dynamics module, while the green solid lines give outline of the ionospheric module. The surface of the Earth is marked by a blue line. The acoustic wave sources used in this study are located at sea level in the "horizontal" center of the atmospheric dynamics mesh (indicated by the open circle in the figure).

meshes are adjusted to match the epicenter of the 2011 Tohoku earthquake as shown in Figure 1; the location of the source of acoustic waves in the model is marked by an open circle in this figure.

The case study pursued here is based on the $M = 9.0$ 2011 Tohoku earthquake, which occurred off of the east coast of Japan (~38.32 N, −42.36 E) on 11 March 2011 at 5:46:22 UTC [e.g., *Tsugawa et al.*, 2011; *Saito et al.*, 2011]. This earthquake occurred during somewhat geomagnetically active conditions ($D_{st} \approx -80$ nT) which is also apparent in TEC and magnetometer data [*Komjathy et al.*, 2012; *Utada et al.*, 2011].

Infrasound sources are included in the neutral dynamics model as sea-level fluctuations in velocity, effectively providing a boundary condition, and are specified as

$$v_z(r, z = 0, t) = Ae^{-r^4/2\sigma_r^4} \sin(\omega t) \left[u(t) - u\left(t - \frac{2\pi}{\omega}\right)\right], \quad (1)$$

where $u(t)$ is the Heaviside step function, which is used to limit the sea surface model to one temporal oscillation. After the disturbance is terminated in the simulation, the sea-level boundary conditions are fixed to satisfy standard reflecting boundary conditions for incident acoustic waves.

The temporal scale, size, and amplitude of the source boundary condition (equation (1) parameters ω, σ_r, and A) have been chosen based on ocean buoy data and reported modeling of the initial sea surface displacement following the 2011 Tohoku earthquake. In particular, *Kakinami et al.* [2012, Figures 2 and 3] suggest large ocean surface perturbations of ~6–8 m in the minutes following the earthquake. Analyses presented in *Mikumo et al.* [2013] suggest a 4–6 m initial sea surface displacement which occurred over a timescale of 3–4 min. *Tsushima et al.* [2011] similarly estimate initial ocean surface upheaval of ~4–8 m. Analysis of ocean-bottom tsunami sensors in *Maeda et al.* [2011] indicated a several meter ocean surface displacement occurring over a 3–4 min time scale. The spatial scale from these studies is not perfectly constrained but may occur over ~0.5–2° of latitude/longitude [*Tsushima et al.*, 2011; *Kakinami et al.*, 2012; *Astafyeva et al.*, 2013a]. Note that this horizontal scale is large enough, compared to mHz acoustic wavelengths, to be fairly directive (a term here used to describe the angular dependence of the acoustic *radiation pattern* in comparison to that of an isotropic "point" source). These published analyses lead us to approximate the velocity of the sea surface response to the 2011 Tohoku earthquake as $A \approx 35$ mm/s with a time scale of $2\pi/\omega = 3$ min and a spatial scale of $\sigma_r = 100$ km. Note that this source is fairly conservative for the 2011 Tohoku event in the sense that it likely underestimates the peak ocean surface displacement (our source has a maximum upward displacement of 2 m).

While the source horizontal extent, amplitude, and timescale have been constrained based on available information in the literature, there are still some uncertainties that could impact our modeling of the atmosphere-ionosphere responses. One such limitation is that there could be source frequencies higher than those encoded by the source function of equation (1), which would tend to increase the directivity, while also generating waves that dissipate at lower altitudes (or potentially form "*N* wave" shocks at lower altitudes, such as observed above strong earthquakes over land, e.g., *Astafyeva et al.* [2013a]). Unfortunately, high-rate GPS data (e.g., the 1 Hz GPS data analyzed in *Astafyeva et al.* [2013b]) do not capture the full relevant spectrum of source frequencies, since TEC is mostly representative of *F* region plasma density in the middle thermosphere

(~250 km), where higher-frequency acoustic waves will already have significantly, if not completely, dissipated. More complete information about the initial ocean surface response spatial and temporal scales could potentially allow these limitations to be more fully addressed in future work.

As a final note, it is emphasized that the source represented by equation (1) is intended to model the initial uplift of the ocean surface in response to the undersea earthquake and *does not* include a subsequent tsunami response nor does it capture the full spectrum of dynamics. Furthermore, it does not account for the three-dimensional nature of the actual disturbance, such as could be provided by a comprehensive ocean surface model simulation. Hence, our results are only intended to model the short-term ionospheric dynamics above the epicenter relevant to acoustic wave generation at dominant periods and do not capture tsunami-generated gravity waves. Despite this, some gravity waves are generated by the upward and downward surface disturbances alone and are present in the numerical results and apparent in the measured TEC data [e.g., *Matsumura et al.*, 2011].

3. Observable Responses of the Atmosphere-Ionosphere System to the 2011 Tohoku-Oki Earthquake

The 2011 Tohoku-Oki earthquake occurred on 11 March 2011 at 5:46:23 UT off of the east coast of Japan at geographic coordinates of 38.32°N, 412.37°E. The corresponding geomagnetic latitude of this earthquake (evaluated with a simple tilted dipole model, e.g., *Huba et al.* [2000], used in our ionospheric simulations) is ~29.1°N.

Our source model has been chosen based on available information about the initial ocean surface response [*Tsushima et al.*, 2011; *Maeda et al.*, 2011; *Kakinami et al.*, 2012; *Mikumo et al.*, 2013]. We also compare model outputs of observable quantities including TEC perturbations and ground-level atmospheric pressure perturbations against available measurements. The 2011 Tohoku earthquake was particularly well observed, and the ionospheric and oceanic responses have been well documented. Hence, it is an important case study to examine in detail the effects of strong ocean surface perturbations at the base of the atmosphere-ionosphere system and provides a reference test for the effectiveness of our nonlinear models.

3.1. Vertical TEC Perturbations

Figure 2 shows the modeled values for vertical TEC perturbations versus magnetic latitude and time above the epicenter. All TEC model results shown in this paper use variation of TEC from background which is computed by subtracting out the TEC value from a control simulation run without any wave forcing. Figure 2a shows a range of magnetic latitudes and times covered by the simulation, while Figure 2b shows vertical TEC traces extracted from three specific magnetic latitudes: one above the epicenter (red line) and two at other nearby latitudes (yellow and blue lines, both removed by ±1 1/4° from the epicenter, respectively). A large, ~−4 TECU depletion (blue colored region) is apparent just south of the epicenter while a smaller enhancement of ~2 TECU (yellow color) exists just northward of the epicenter. Similar to results presented and discussed in *Zettergren and Snively* [2015], the larger magnitude perturbations (viz., depletions) appear in the direction of the magnetic equator. In addition to the longer lived features, infrasonic (3–4 min period) perturbations in the TEC are present throughout the event. These oscillations begin around the time of the apparent ionospheric onset of the event (5:58 UT) and intensify again at around 6:20 UT. The second "burst" of 3–4 min oscillations is, we will demonstrate, an effect of reflection. Vertically propagating acoustic waves generated by the source reflect off of the thermospheric temperature gradient and then again off of the tropopause and sea surface before returning to the thermosphere, forming a second train of dispersed, upward propagating waves well after the ocean source has been removed from the model. Likely, the similar amplitudes between the two bursts of waves indicates saturation in the acoustic wave field of the first burst, which will be discussed further in section 4.2.

Also shown in Figure 2, panels c and d are GPS ionospheric TEC measurements for the 2011 Tohoku event. Absolute TEC values used to construct this plot were obtained from the same algorithm and software as used in *Galvan et al.* [2012]. However, it is important to note that our presentation and analysis differs from *Galvan et al.* [2012] in that *we do not bandpass filter our data*, whereas they use a 0.5–5 mHz bandpass filter. Instead, we retain features of the longer-term trends (viz., depletions) and perform a simple background subtraction as follows. For each satellite-receiver pair, a variation from background is computed by subtracting out the measured TEC value for each at 5:45 UTC (about a minute prior to the earthquake). This method does not

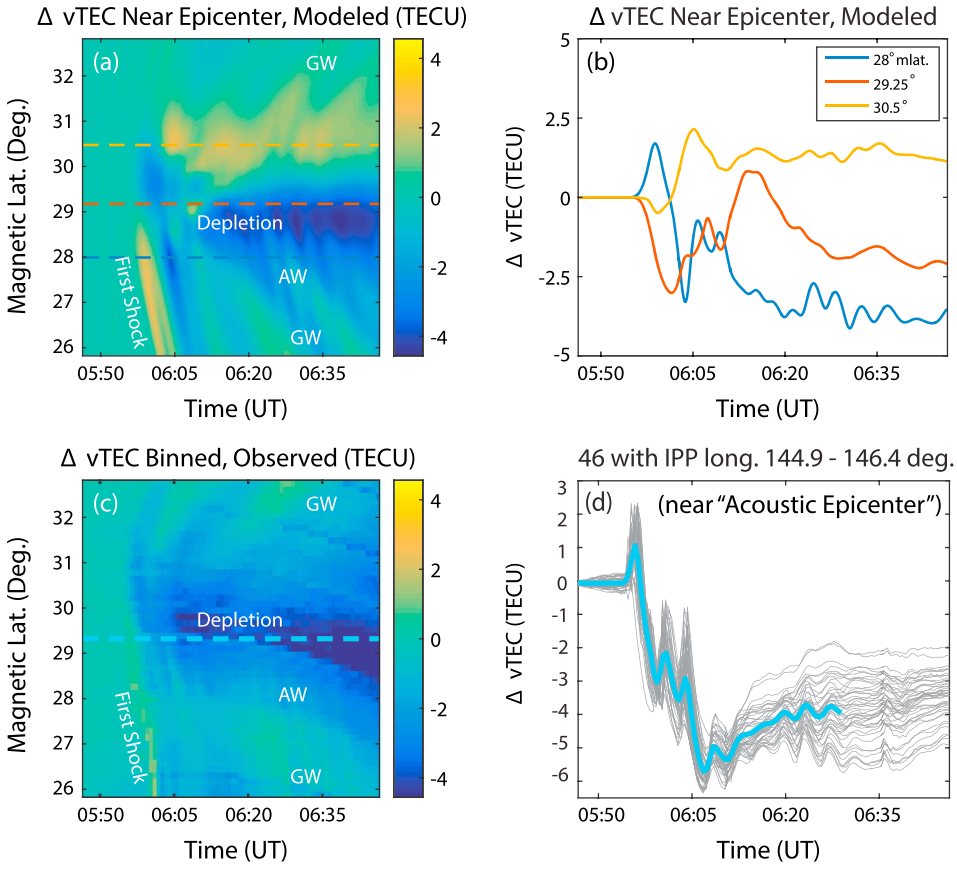

Figure 2. Simulated and observed TEC perturbations from 2011 Tohoku case study. TEC signatures related to acoustic waves (AW) and gravity waves (GW) are indicated in the Figures 2a and 2c. (a) Simulated vertical TEC perturbations (background subtracted) versus magnetic latitude and time. The location of the Tohoku epicenter is marked by a red line, while other latitudes of interest are marked by yellow and blue lines, respectively. (b) Simulated TEC perturbations versus time extracted from select magnetic latitudes (near the epicenter and $\pm 1\frac{1}{4}°$ from the epicenter). The latitude from which each TEC trace is extracted is indicated by the dashed line of the same color in Figure 2a (the locations are also indicated in the legend). (c) Unfiltered TEC data, from satellite GPS26 and multiple stations, binned according to latitude and UT for comparison to Figure 2a. (d) TEC data from select stations (paired with satellite GPS26) that are nearest, on average, to the center of the observed ionospheric depletion. These are compared, in the text, to the model output in Figure 2b.

account for background trends in TEC, but we have obtained similar results using a moving average filter to compute background so our results are not greatly dependent on detrending method.

Since the ionospheric pierce points (IPPs) of GPS satellite-station pairs move with time, some additional post-processing is needed for a meaningful comparison between data and modeled TEC. This issue is addressed by binning TEC data for a given time interval by IPP latitude so that they are directly comparable to the model output which uses a *fixed* latitude grid. For this study we use 30 s temporal bins and 50 IPP latitude bins covering a range of ±3.5° about the epicenter (bin width of about 0.14°). All data shown in Figure 2 are from satellite GPS26, which has IPPs nearest to epicenter during the event. Data are used from all stations which have at least one record with an IPP within ±2° of longitude of the epicenter location, but our results are not overly sensitive to the choice of longitude range. Bin-averaged elevation angles for these observations range from ~18 to 55° and are roughly 35° for the bins near the time and location of the TEC depletion. All bins shown in Figure 2 have at least one measurement, while the time and location bins corresponding to the depletion generally have ~5–30 samples per bin. The results of the binning of these data are shown in Figure 2c which indicates the latitude of the epicenter by a light blue dashed line.

The binned GPS data in Figure 2c clearly illustrate the formation of a TEC depletion of about −4.5 TECU around the epicenter region. The depth of this depletion closely matches what is seen in the model results in Figure 2a. The location of the depletion, however, seems to be more southward of the epicenter in the

simulations versus roughly centered about the epicenter in the data. In addition, shortly after the onset of the event a +2 TECU enhancement propagates southward at speeds similar to the thermospheric sound speed. Also to the south of the epicenter, two bursts of 3–4 min period (infrasonic) propagating structures are seen centered around ~6:05 UT and ~6:25 UT. Both of these features very closely match the simulation results in terms of amplitude, speed, and onset time. Lower frequency propagating features can be seen to both the north and south of the epicenter, which appear consistent with gravity waves such as reported by *Matsumura et al.* [2011] that are generated simultaneously to the initial disturbance. These are most apparent around 2° north of the epicenter in both the model and data (Figures 2a and 2c). The model results show a TEC enhancement north of the epicenter, while the data indicate no such enhancement.

In addition to the binned data, TEC traces from station-satellite pairs near the region of strongest ionospheric response are shown in Figure 2d. This region corresponds to a longitude range of 144.9–146.4° and a latitude range of roughly ±0.5° about the epicenter. In this panel, the individual station traces are grey, while the average over all stations in this group is shown by a light blue thick line. This average is generated by interpolating data from each station to a common time basis prior to averaging. Figure 2d shows the strong decrease in TEC following the earthquake (apparent in the binned data) and also illustrates an additional feature that is not easily visible in the binned data. The TEC depletion is followed by a small upward trend (lasting 7–10 mins) centered around 6:02 UT. This longer time scale feature is very similar in character to the model results south of the epicenter (the blue line in Figure 2b) as it occurs at about the same time and is superposed on top of infrasonic oscillations. The longer period feature is later discussed in the context of the ionospheric-thermospheric responses to the dissipation of a steepened acoustic shock wave (here resulting from merging of two leading wave fronts), and subsequent oscillations, produced by the initial ocean surface upheaval.

The primary features of the TEC observations from the 2011 Tohoku earthquake, specifically the initial acoustic shock enhancement, subsequent TEC depletion ("hole"), and arrivals of acoustic wave packets that are delayed by partial reflection below the thermosphere, are also apparent in the model simulation results. The agreement with the simulation is indeed quite good to the extent that it captures the detailed infrasonic phase structures in both the time-latitude plots Figures 2a and 2c and the single latitude/station traces in Figures 2b and 2d. The modeling and unfiltered data presented in Figure 2 are also consistent with TEC perturbations published in several previous studies [*Saito et al.*, 2011; *Kakinami et al.*, 2012] noting strong TEC depletions several minutes after the 2011 Tohoku earthquake.

As noted above, the main inconsistency between the model and data is the northward TEC enhancement, which appears in the model but not data. The source of this inconsistency may be due to one or more assumptions in the modeling or data analysis, which we believe can be addressed effectively in the future with a high-resolution 3-D description of the source, winds, and atmosphere-ionosphere response. There is also evidence in the TEC data that there may be significant longitudinal structure in the ionospheric response, a characteristic we plan to examine in detail in future studies, which may indicate a combined effect of winds, 3-D source directivity, and 3-D observing geometry. Note that the observed TEC depletion migrates further southward over time and the observed gravity waves (longer period signatures propagating away from epicenter) exhibit apparent asymmetry about the epicenter; this may imply ambient meridional winds that cannot be captured within our axisymmetric model. Furthermore, the ocean surface disturbance in reality exhibited asymmetry that cannot be captured in two dimensions [e.g., *Mikumo et al.*, 2013], in addition to higher- and lower-frequency spectral components. The presence of somewhat higher-frequency acoustic waves could thus also increase the effective directivity of the source, possibly reducing the northward transport effects that accompany the formation of the hole. The 2-D ionospheric slice through a 3-D symmetric acoustic wave field is also a model assumption that may enhance effective meridional transport and contribute to differences between the data and simulations.

Even though a given TEC signature is insufficient to uniquely characterize an ocean source, the agreement of model output TEC and data (in terms of the depth of the depletion and infrasonic fluctuations) indicates that our source *amplitude* within this bandpass is likely quite comparable to that of the ocean surface response to the 2011 Tohoku earthquake. The exact source *spectrum* is more difficult to determine, as it is not fully resolved in either model nor data; however, this matters less in an ionospheric context since dissipation of the infrasonic waves in the thermosphere will tend to filter waves with periods shorter than ~1 min by the time they encounter the *F* region ionosphere (where the largest density perturbations are generated).

The GPS TEC signatures are also spatially filtered by vertical integration, thus further limiting the observability of shorter-period acoustic waves.

3.2. Ground-Level Magnetic Field Fluctuations

Magnetic field perturbations, produced by the acoustic wave driven dynamo currents, can also be calculated by our coupled models [*Zettergren and Snively*, 2015, Appendix A]. Several studies of magnetic fluctuations associated with the 2011 Tohoku earthquake indicate some levels of activity (several nT perturbations) associated with the event [*Hao et al.*, 2012, 2013]. Our model results indicate ±4 nT vertical magnetic field perturbations on the ground near epicentral latitudes, reasonably consistent with the amplitudes suggested by observations. Future work will further examine these perturbations and their connections to magnetic observations following the 2011 Tohoku earthquake.

3.3. Ground-Level Pressure Perturbations

Ground-level microbarograph measurements from distances of hundreds to thousands of kilometers from the epicenter indicated significant pressure fluctuations (tens of Pa) following the Tohoku earthquake. *Arai et al.* [2011] show 20–60 Pa PTP (peak to peak) perturbations at a distance of ~250 km from the epicenter. This signal was time delayed from the onset of the earthquake by about the acoustic wave travel time between the epicenter and station. *Arai et al.* [2011] attributed these perturbations to Lamb waves generated by the initial ocean surface response to the earthquake and estimated the wave group velocity as 311 m/s. Measurements from other regional microbarographs (~1500 km or less from the epicenter) showed ~10–20 Pa PTP pressure fluctuations and were similarly time delayed from the earthquake onset, indicating that these waves originated from the initial ocean surface upheaval, as opposed to being generated locally by seismic waves in the Earth's crust. Observed periodicities were roughly in the ~2–5 min range [e.g., *Arai et al.*, 2011, Figure 2; *Mikumo et al.*, 2013, Figure 3].

Our simulations do not fully capture the boundary (Lamb) wave since there is no horizontal component of wave velocity—neither phase nor fluid velocity—at the bottom of the domain where the source is included nor do any resulting tsunami disturbances propagate through the base of the model to enable a continued disturbance or generation of traveling tsunamigenic gravity waves. However, our simulated pressure fluctuations (not shown) just above the epicenter are ~20 Pa. This is similar in amplitude to the reported microbarograph observations from several hundreds of kilometers away from the epicenter of the earthquake and serves as further evidence that our source likely *does not overestimate* the amplitude of actual ocean surface response.

4. Modeled Atmosphere-Ionosphere Dynamics Above the 2011 Tohoku-Oki Earthquake

The apparent agreement between observable model outputs and measured data (outlined in previous sections) invites detailed analysis of some *unobservable* aspects of the ionospheric and thermospheric responses during the 2011 Tohoku event. Data-model agreement for the 2011 Tohoku event serves as a critical calibration point for an *M*9.0 undersea earthquake source, which motivates the study of the amplitude dependence of the ionospheric response in section 5.

4.1. Ionospheric Response Dynamics

Figure 3 (and the corresponding movie included with the supporting information) shows the ionospheric electron density and velocity responses at three different times (5:58:52 UT, 6:01:12 UT, and 6:03:22 UT) near when the TEC depletion (shown in Figure 2) begins to form. Figures 3a, 3d, and 3g show the density versus altitude and magnetic latitude, while Figures 3b, 3c, 3e, 3f, 3h, and 3i show density and radial velocity (positive upward) profiles, respectively. These quantities were extracted from three different latitudes near the epicenter corresponding to the three color-coded, dashed lines in Figures 3a, 3d, and 3g. Finally, the black dashed line in Figures 3b, 3c, 3e, 3f, 3h, and 3i shows profiles from a control simulation (which does not include an ocean source of acoustic waves) extracted from directly above the epicenter. These control profiles provide a convenient reference for comparisons.

The *F* region density accompanying TEC perturbations shown in Figure 3 is quite large (several tens of percent in many cases), and these density perturbations partially cancel during the vertical TEC integrations. Hence, the TEC perturbations (which are ~ 10–20%) do not fully capture the severity of the distributed ionospheric response. Very steep layered profiles, up to 60–70% density increases over control simulation, e.g., Figure 3i,

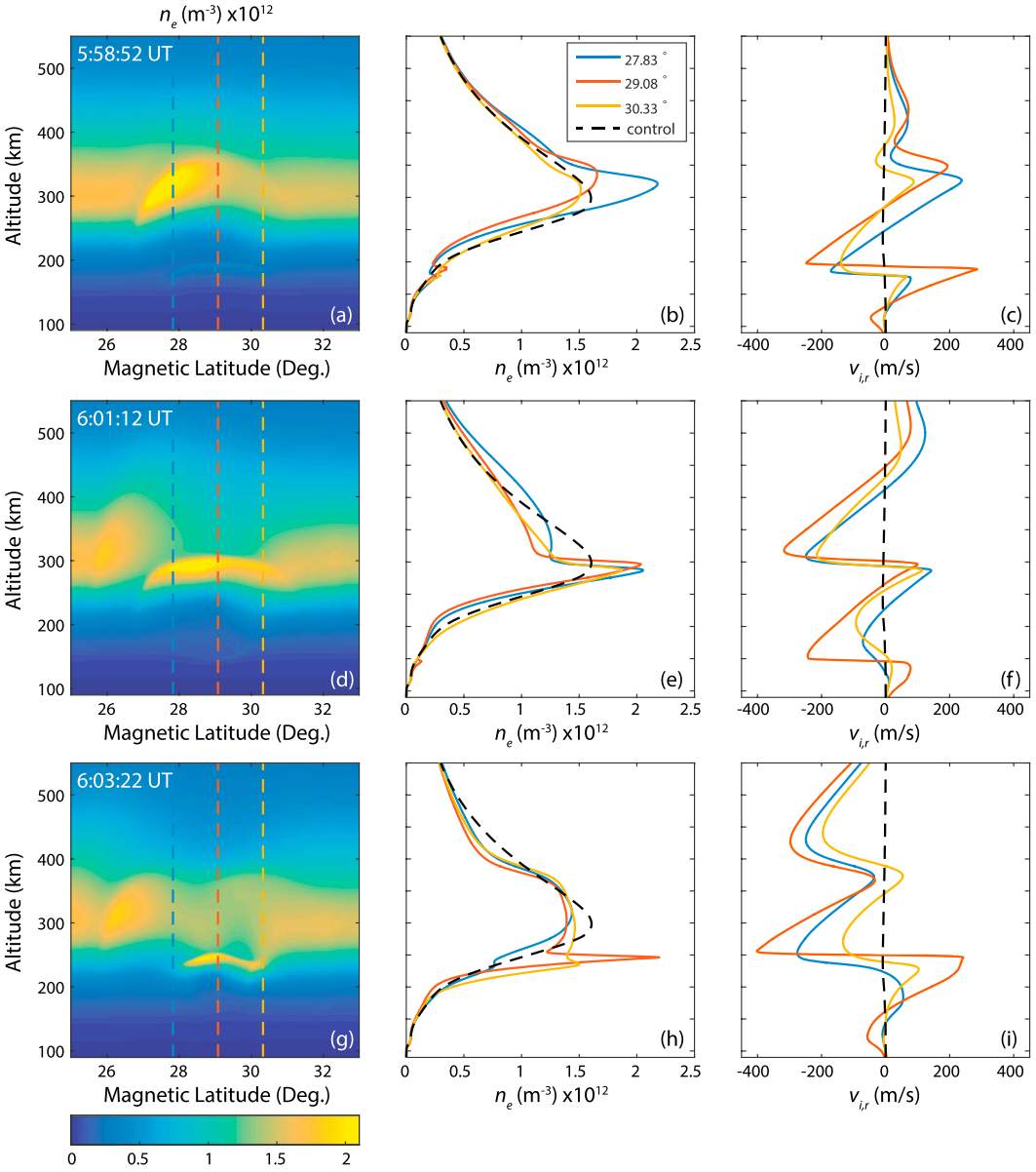

Figure 3. Simulated ionospheric density and velocity responses at different times over the epicenter for the 2011 Tohoku case study. Each row of figures represents a snapshot in time (as marked in the first panel of each row). (a, d, and g) Electron density versus altitude and magnetic latitude. (b, e, and h) Electron density profiles extracted from the three locations with corresponding line colors in Figures 3a, 3d, and 3g. The dashed black line shows what the electron density over the epicenter would be in absence of a perturbation (a control simulation). (c, f, and i) Vertical ion velocity extracted from three locations corresponding to the dashed lines in Figures 3a, 3d, and 3g (the control simulation velocity is, likewise, shown as a black dashed line in these plots).

250 km altitude, form during passage of steep acoustic waves. Layers similar to these may have been observed via digisonde following the 2011 Tohoku earthquake [*Maruyama et al.*, 2011; *Maruyama and Shinagawa*, 2014], revealing bottomside ionospheric structuring at higher resolution than captured via GPS TEC. Also, depletions of 25–40% occur during the "downward" phase of wave velocity perturbations, as seen in, e.g., Figures 3b and 3c, 200–300 km; Figures 3e and 3f, 300–400 km; and Figures 3h and 3i, 350–450 km altitude. At the end of the simulation the depletion to the south and enhancement to the north are visible in the *F* region densities; this can be most easily seen in the simulation movie included with the supporting information for this article.

The depletions in ionospheric density occur when the strongest part of the infrasonic wave, illustrated by the times chosen for the plots in Figure 3, forces significant downward and northward ionospheric transport.

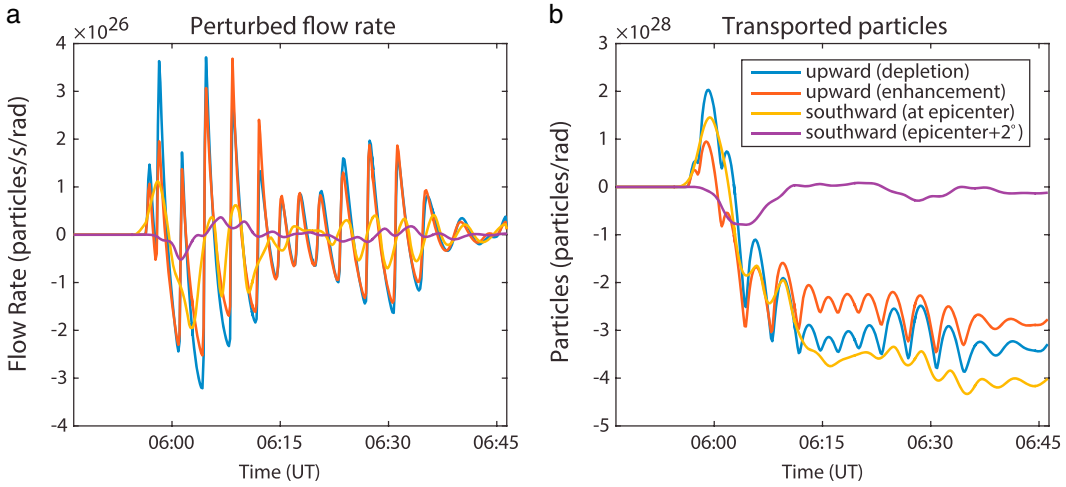

Figure 4. Transport of ionospheric plasma through four surfaces near the epicenter. (a) Flow rates and (b) total number of particles transported through surfaces. In these panels the blue lines correspond to a surface with a vertical normal, located at 300 km altitude, extending −1.08° from the epicenter of the event (roughly corresponding to the region of the TEC depletion). The red lines corresponds to a surface with a vertical normal, at 300 km altitude, extending from +1.08° from the epicenter (the TEC enhancement). The yellow lines correspond to a surface with a southward normal, located at the epicenter, extending in altitude from 200 to 400 km. The purple lines correspond to a surface with a southward normal, located +2° from the epicenter, extending in altitude from 200 to 400 km.

This motion is caused by the strong downward neutral velocity that, through ion-neutral drag, generates a downward, field-aligned motion in the plasma having geographic northward and downward components. Downward motion will tend to result in enhanced charge exchange of O^+ since the plasma is transported to an altitude where molecular constituents (in particular N_2) are more dense. The effect of the downflow is, then, a conversion of O^+ into molecular ions. Molecular ions recombine more readily than O^+ and a net depletion of plasma is created. Generally speaking, this process would occur to some degree in response to any nonequilibrium downward motion. The horizontal (i.e., northward) transport will generate a density change if there is a divergence in particle flux.

Figure 4 summarizes the salient features of northward and downward O^+ transport during the 2011 Tohoku event simulation. Figure 4a shows flow rates (particles/s/rad) computed through four different surfaces near the epicenter of the event. The first (blue lines) has a vertical surface normal, is located at 300 km altitude, and extends −1.08° from the epicenter of the event (roughly corresponding to the region of the TEC depletion). The altitude of this surface (300 km) is near the nominal *F* region peak, below which the plasma density is governed by production and loss as opposed to transport [*Garriott*, 1969]. The second (red lines) also has a vertical normal, is located at 300 km altitude, and extends +1.08° from the epicenter (the TEC enhancement). The third (yellow lines) has a southward normal, is located at the epicenter, and extends in altitude from 200 to 400 km (encapsulating the *F* region peak). The fourth (purple lines) has a southward normal, is located +2° from the epicenter (toward the region with the TEC enhancement), and extends in altitude from 200 to 400 km. The upward flow rates shown in these figures (F_r) are given by

$$F_r = \int_{\theta_1}^{\theta_2} n\mathbf{v} \cdot \hat{\mathbf{e}}_r r_0^2 \sin\theta \mathrm{d}\theta \tag{2}$$

while the southward rates (F_θ) are

$$F_\theta = \int_{r_1}^{r_2} n\mathbf{v} \cdot \hat{\mathbf{e}}_\theta r \sin\theta_0 \mathrm{d}r \tag{3}$$

In these equations $n\mathbf{v}$ is the perturbed ion number flux, r is the radial distance from the center of the Earth, θ is the polar angle coordinate for a spherical system centered on the Earth (increasing toward the south pole), $\hat{\mathbf{e}}_r$ is a unit vector in the radial direction, $r_0 = 300$ km, and θ_0 marks the polar angle (and latitude) of the surface through which southward flow is calculated. Figure 4b shows a quantity proportional to the total number of particles transported through these surfaces (particles/rad due to the 2-D model). These quantities are computed as the time integral of the flow rates listed above.

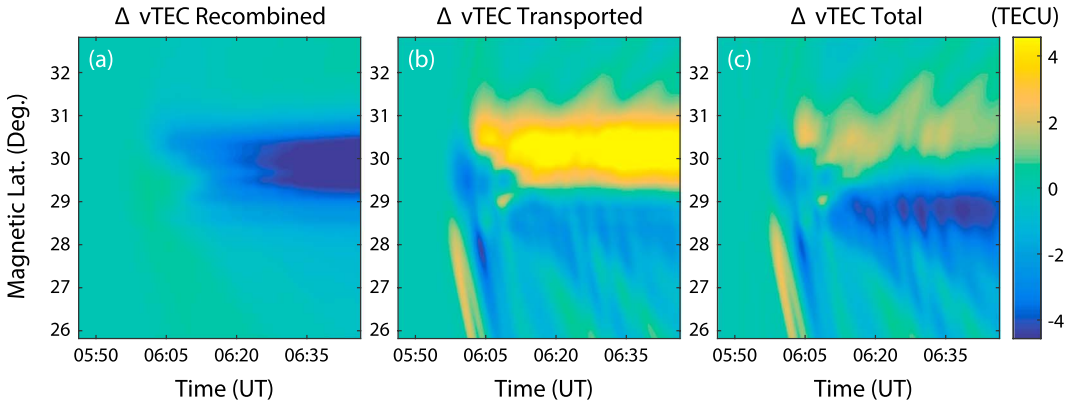

Figure 5. Contributions of plasma loss (i.e., recombination) and transport to modeled variation in vTEC. (a) TEC variations due to plasma loss. (b) TEC variations from transport. (c) Summed loss and transport variations. Note that this panel closely matches the simulated vTEC perturbations in Figure 2a.

Analysis in Figures 4a and 4b shows that the ionosphere is initially lifted upward during the event (the positive particle count in Figure 4b from ~5:56–6:02 UT) and then depressed downward (the negative counts following ~6:02 UT). Both regions (above the depletion in blue and enhancement in red) experience predominantly downward particle transport following 6:02 UT, though this downward transport effect is slightly larger to the south of the epicenter. The transport at the epicenter is largely northward (Figure 4b, yellow line) while there is very little net particle transport through the surface to the north of the epicenter (Figure 4b, purple line). Hence, there is a net convergence of flux to the north of the epicenter, which will tend to deplete the region to the south while creating an enhancement to the north. At the same time, the ionosphere in both regions is being forced downward, which tends to cause more recombination and deplete the plasma.

Figure 5 illustrates relative contributions of loss and transport to vTEC variations simulated for the 2011 Tohoku event (note that background vTEC variations from each source have been subtracted out using the control simulation). To generate this comparison, terms from the electron continuity equation encapsulating loss and transport of plasma (specified by the model output) were integrated in time and with respect to altitude to form TEC variations due to each of these processes. Figure 5a depicts TEC variations due to plasma loss (viz., recombination—more recombination than in the control simulation results in a negative value), Figure 5b shows loss due to transport (viz., flux divergence—a negative value indicates more TEC loss than in the control simulation), and Figure 5c shows the sum of these two vTEC variations. Figure 5a shows that the northward and downward transport (as illustrated in Figure 4 and associated discussions above) results in plasma being pushed downward and to the north of the epicenter resulting in strong plasma recombination and loss from latitudes of (28.5–30.5° magnetic latitude). Figure 5b shows that northward and downward transport supports a strong flux divergence to the south of the epicenter and convergence to the north. Note that the sum of loss and transport terms (Figure 5c) is very close to the full TEC variations computed from the simulation and shown in Figure 2, indicating that recombination and transport are the dominant processes leading to the TEC variations in the model (viz., changes in production between the control and 2011 Tohoku simulations are not significant). Combined effects of recombination and inflow to the north results in a somewhat muted enhancement of TEC in this region (Figure 5c) and strong depletion in the region where both loss and outflow act in concert (magnetic latitudes of 28–29°). The depletion south of the epicenter is stronger than the enhancement to the north because the depletion results from coordinating processes (outflow and recombination) rather than competing processes (inflow versus recombination).

4.2. Thermospheric Acoustic Wave Dynamics

The thermospheric state corresponding to the ionospheric response of Figure 3 is shown in Figure 6 (which has a corresponding movie included with the supporting information). In this figure the columns show different state parameters, while the rows are snapshots of model output at different times. Figures 6a, 6d, and 6g show the neutral velocity in the vertical direction. This component is responsible for most of the ionospheric density and TEC response character—particularly the long-lived TEC depletion. This strong downward velocity, when projected along the geomagnetic field line, generates the strong northward and downward transport

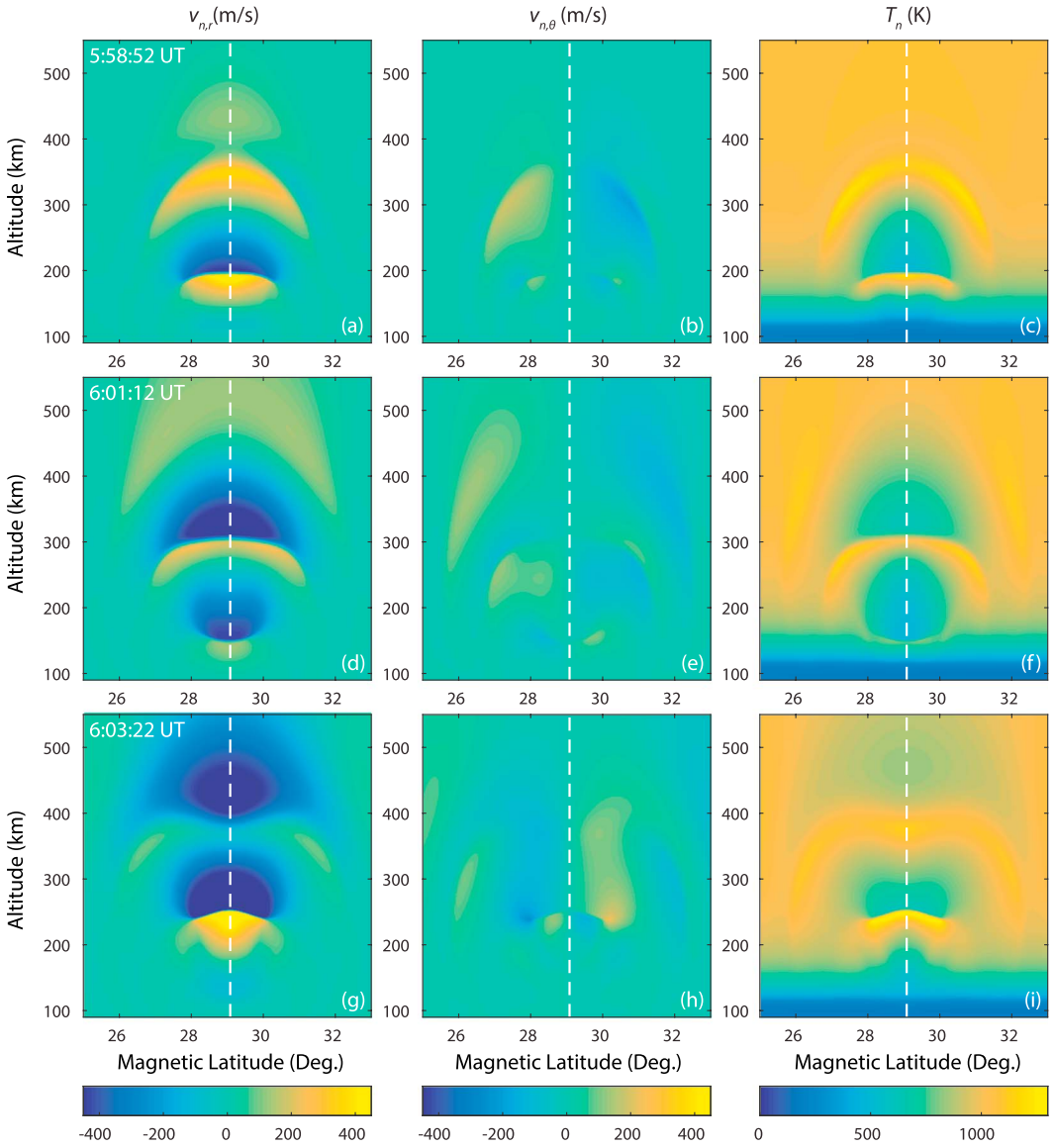

Figure 6. Simulated thermospheric responses at different times for the 2011 Tohoku case study. Each row of figures represents a time snapshot in time (the time is marked in the first panel of each row). (a, d, and g) Radial (vertical) neutral velocity over magnetic latitude and altitude. (b, e, and h) Horizontal (positive southward) neutral velocity over magnetic latitude and altitude. (c, f, and i) Neutral temperature perturbation over magnetic latitude and altitude. The vertical dashed lines in each panel mark the epicentral latitude.

apparent in the ionospheric simulation results (Figures 3 and 4). Figures 6b, 6e, and 6h show the horizontal velocity, which is generally much weaker than the vertical velocities of these waves. Figures 6c, 6f, and 6i show neutral temperature as it is perturbed by the dissipating acoustic waves.

Figure 6 illustrates the nonlinear nature of the atmospheric response to ocean forcing similar to that present during to 2011 Tohoku earthquake. Velocities exceeding 400 m/s and temperature perturbations exceeding 300 K are present over a ~2° range of latitudes during the passage of the strongest part of the infrasonic wave (~6:01–6:05 UT). The largest-amplitude part of the wave steepens aggressively during propagation through the 200–250 km altitude region and dissipates (smooths) noticeably at higher altitudes. For example, in Figures 6a and 6b (5:58:52 UT) at ~200 km altitude a steep phase front is seen to exist. This front propagates upward and becomes more diffuse by the time it reaches 400 km at 6:03:22 UT. At 6:03:22 the wave exhibits mostly downward field-aligned velocity (corresponding to negative $v_{n,r}$) which is responsible for downward and northward transport in the ionosphere resulting in the formation of the TEC depletion. Phase fronts of the

strongest parts of the wave distort noticeably during upward propagation, further complicating the thermospheric and ionospheric responses shown in Figures 3 and 6. For example, the front at 150 km at 6:01:12 UT is concave upward and distorts to concave downward at 6:03:22 UT—features particularly visible when viewing the simulation movies including in the supporting information.

In the simulations shown in this paper, nonlinearity of the thermospheric acoustic waves (apparent in the steepness of the wave fronts in the velocity panels of Figure 3) and their subsequent rapid dissipation by viscosity play key roles in producing the TEC peak upon initial arrival of the waves and the subsequent depletion in Figure 2 and as discussed earlier. Analysis of neutral transport rates (not shown but similar to what was done for the plasma in Figure 4) reveals that upward oxygen transport follows a pattern very similar to the upward plasma transport shown by the blue and red lines in Figure 4b. Oxygen is initially transported upward and then falls down resulting in net downward oxygen transport over most of the duration of the first arriving waves. From a neutral dynamics standpoint, the initial nonlinear waves result in upward oxygen transport; this is followed shortly after by the strong downward flow, superposing the effects of a downward acoustic velocity following the positive shock and lack of buoyancy following upward transport. (Note that, in general, the competing importance of compression and buoyancy/gravity in the thermosphere's response and recovery will depend on the amplitudes and time scales of the waves or shocks, their dissipation, and the ambient state of the thermosphere.) These wave dynamics, coupled with strong viscous dissipation, result in predominantly downward neutral transport velocities at 6:00–6:04 UT in the altitude ranges of 150–375 km in Figure 6d and above 250 km in Figure 6g.

The time scales of the transport are approximately related to the packet duration and are thus longer than the wave period. The merging of acoustic fronts furthermore produces some conversion to longer-period nonlinear features, such as the first arriving shock, which comprises a dispersed leading phase front that has merged with a larger-amplitude phase front behind. The strength of the subsequent downward neutral flows in the Tohoku case study, and more prominently in the stronger (two times) case study discussed in section 5, are sufficient to slow the next arriving wave front and allow it to be overtaken by and merge with its successor, thus further enhancing downward flow. The strong neutral downflow that results in the plasma transport summarized in Figure 4 leads to the formation of a TEC depletion. Note that the times shown in Figure 6 clearly correspond to when the depletion in TEC starts to appear in Figure 2. Also note that the apparent multiple depletions measured in Figure 2d further support this explanation, where a sequence of strong, merged fronts produce two "steps" (at times of ~5:58 and 6:04 UT) that each contribute to deepening the depletion.

The reflection processes that ultimately lead to apparent acoustic resonance are also present in our simulations (cf. also *Matsumura et al.* [2011] for another modeling example of this process). The wave is partially reflected between the thermosphere, tropopause, and ground, and the resulting dispersion and propagation delays lead to the formation of two extended acoustic packets ("bursts"), despite having been forced only by a single oscillation. The arrival times and durations of these events are determined by multiple partial reflections that occur within the atmospheric structure and are consistent for both the first and second bursts of acoustic wave packets identified in the TEC data. The fact that both bursts have similar oscillation amplitudes, i.e., see Figure 2d and detailed discussions in section 5, likely indicates saturation in the acoustic wave field during the first burst. Thus, the oscillations within the first burst are limited in amplitude by nonlinearity and dissipation, which also indicate their significant potential impact on transport. By comparison, the second burst exhibits a coherent waveform at similar amplitude to the first in the doubled-amplitude case (approximately hundreds of m/s compressional vertical velocities) but with less impact on transport (limited contribution to the depletion).

The amplitudes of the acoustic waves and the coherence of the subsequent vertical reflections and resonant buildup are enhanced by the directivity of the wave source. This is due to the large source region relative to the acoustic wavelength in the lower atmosphere; the sea surface displacement, effectively acting as a large piston, spans a radial extent ~100 km. As with the radially extended directive source used in *Zettergren and Snively* [2015], the directivity is notably greater than a compact "piston" or a spherical point source radiator. This leads to considerable amplitudes of the waves at high altitude, as they are not limited by a $1/z$ geometric factor. Nor are the waves a perfect beam, and the phase fronts do spread radially and experience further refraction, leading to curvature, as they are incident on the base of the thermosphere (see Figure 6).

Even at these large amplitudes it is important to appreciate that, consistent with *Zettergren and Snively* [2015], $Kn < 0.1$ is satisfied at grid scale for altitudes below ~380 km and at the wavelength scale below ~550 km.

Steepened wave and dissipating shock scales are larger than grid scale above ~300 km, and the effective Knudsen number $Kn < 0.1$ (and typically $\ll 0.01$) throughout the duration of the simulations. Thus, the Navier-Stokes assumptions of continuum are not violated [e.g., *Brown*, 1996]. The steepened wave scales approach the grid scale only at altitudes where they are still physically described by the model system of equations; although the shock fronts in this altitude range are underresolved, they are captured conservatively by the numerical scheme (based on the shock-capturing finite volume method of *LeVeque* [2002] and *Bale et al.* [2002] as discussed in section 2 and by *Zettergren and Snively* [2015]).

Finally, it is worth noting that wave-like (but nonwave) perturbations do persist up to the nominal altitude of the model exobase >500 km, albeit at reduced amplitude due to viscous dissipation, where the continuum assumptions of the Navier-Stokes atmospheric model do begin to break down. The effective Knudsen number over the acoustic wave scales approaches ~1 at top of the domain, so this transitional region must be considered a "numerical domain." As a beneficial result, we are able to perform all simulations with simple outflow boundary conditions and without a sponge layer, thus minimizing boundary interactions. Collisional ionospheric coupling is very weak at these highest altitudes, and this region thus also provides a smooth and continuous transition between neutral and ionospheric model domains.

5. Amplitude Dependence of Responses

Three additional simulations are presented in this section to investigate the response of the atmosphere-ionosphere system to undersea earthquake sources (i.e., of the form of equation (1)) of varying amplitudes. The amplitudes specified are as follows: $A = 0.35$ mm/s (1/100 × the simulated Tohoku amplitude), $A = 3.5$ mm/s (1/10 × the simulated Tohoku amplitude), and $A = 70$ mm/s (2 × the simulated Tohoku amplitude). The location of the source (off of the coast of Japan), the periodicity, and amplitude spatial envelope ($e^{-r^4/2\sigma_r^4}$) are kept constant for purposes of comparison with the Tohoku case study above. This set of sources is not intended to model any particular events but is, instead, chosen to explore a range of reasonable and observable atmosphere-ionosphere responses to undersea earthquake disturbances.

Figure 7 show TEC fluctuations versus magnetic latitude and time for the three additional simulations, which vary the amplitude of the source of equation (1) (in addition to the reference 2011 Tohoku simulation). All of the cases show asymmetry between the TEC response northward and southward of the epicenter (the strongest perturbations, which are negative, are in the southward direction). The strongest case run (2 × Tohoku) has a response with a character very similar to the Tohoku case study above, i.e., a long-lived depletion superposed onto infrasonic frequency perturbations. However, the amplitude of the TEC depletion (~−7 TECU) in this case is not double that of the Tohoku case (which has ~−4.4 TECU), so there appears to be a minor saturation of the semipermanent TEC response, in addition to the acoustic oscillations, at these exceptionally large source amplitudes. The 1/10 × Tohoku case likewise exhibits a much milder form of the hysteresis of the larger amplitude responses (viz., a long-term TEC depletion), while the 1/100 version shows very little long time scale response. The onset of acoustic resonance following reflection is apparent in all of the simulations performed for this paper, but it is most clear in the 1/10 and 1/100 cases due to the relative lack of nonlinear, semipermanent TEC responses. The 1/100 case has TEC perturbations has ±0.02 TECU and is likely close to the unambiguous detectability limit for modern GPS instruments and processing schemes.

The modeled TEC responses are apparently consistent with recent surveys of observed TEC responses for earthquakes of different magnitudes. *Perevalova et al.* [2014] have indicated fluctuations of about 0.07–0.28 TECU for M7.0–8.0 earthquakes occurring during quiet conditions. This is somewhat similar in range to our 1/100 and 1/10 cases which are, according to our scaling of the source amplitude, representative of M7.0 and M8.0, respectively. However, a detailed comparison is well beyond the scope of this paper since these data were collected under differing conditions (geomagnetic, solar zenith angle, season, etc.), span several different types of earthquake focal mechanisms, and include both inland and undersea earthquakes. It is also worth noting that we have focused on the acoustic responses, whereas many of the observations presented in *Perevalova et al.* [2014], particularly for the offshore undersea earthquakes, may correspond to TEC fluctuations also induced by subsequent gravity wave disturbances.

Another recent study that admits comparison to the model results in Figure 7 is that of *Kamogawa et al.* [2015], which compares the character of the ionospheric TEC response (viz., whether any depletions are detectable) during several large magnitude undersea and inland earthquakes. The undersea earthquake examined in this paper results in sea surface displacements of tens of centimeters [cf. *Kamogawa et al.*, 2015, Table 1] and

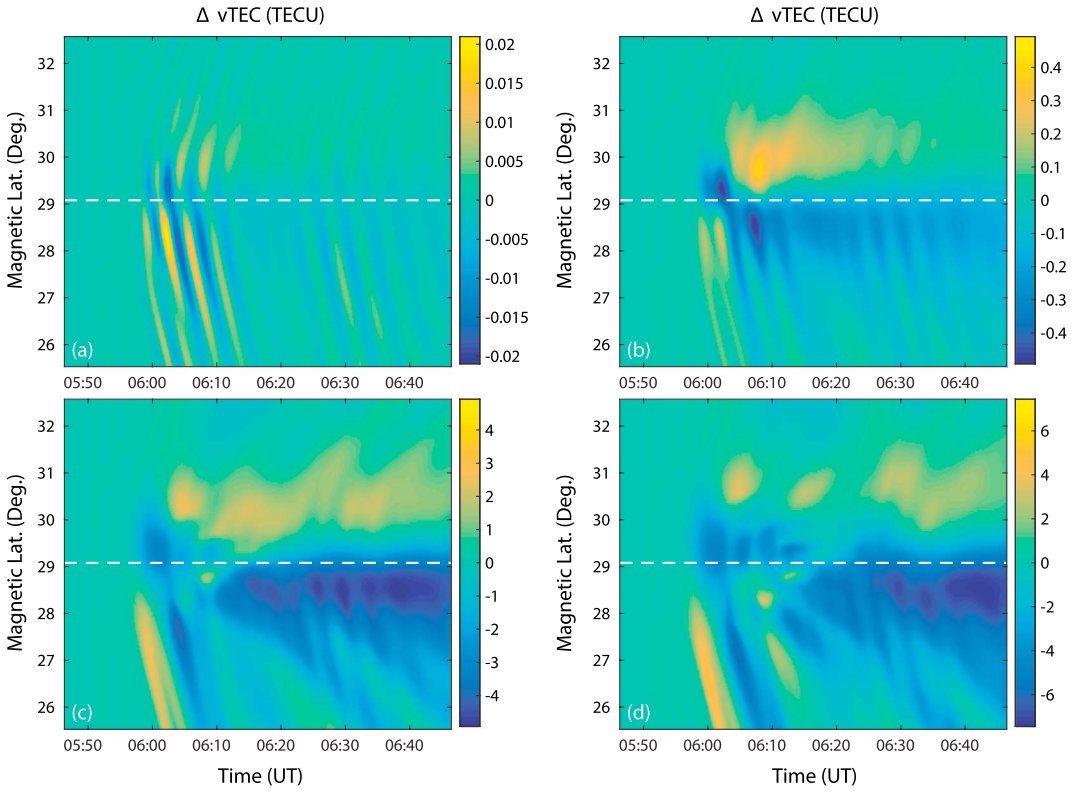

Figure 7. Simulated TEC perturbations to sources of different amplitudes. Simulations with sources that are (a) 1/100×, (b) 1/10×, (c) equal, and (d) double to the estimated amplitude of the 2011 Tohoku earthquake sea surface response, as introduced in the case study in Figure 2, respectively. The horizontal dashed lines in each panel mark the epicentral latitude.

observable vertical TEC depletions (in the range of ~0.1–1 TECU). Our 1/10 Tohoku source had a maximum displacement of about 20 cm, and there is a noticeable vertical TEC depletion to the south of epicenter (about −0.3 TECU; see Figure 7b). It is worth noting that our modeling indicates that forcing the atmosphere with a significantly smaller source than the 1/10 × source does not result in a TEC depletion (cf. Figure 7a).

The amplitude dependence of the thermospheric response is illustrated at a fixed time in Figure 8. Here profiles of vertical neutral velocity and temperature are extracted along the *center geomagnetic field line of the simulations* at 6:03:22 (near the time when the maximum infrasonic amplitude is achieved). The nonlinear effects discussed in the context of the Tohoku case study, leading to large-scale downward flows in the 250–500 km altitude range, are only prevalent in that case study (labeled 1) and the 2 × Tohoku example (labeled 2). These features are associated with the TEC depletions shown in Figures 2 and 7. Velocities for the largest 2 × Tohoku case exceed 600 m/s (superposing both the downflow and embedded acoustic waves), are ~100 m/s for the 1/10 × case, and approximately tens of m/s for the 1/100 × case. Temperature perturbations for the two strong cases approach 25–40% of the background temperature and are largely negative at this time and would decrease the sound speed, leading to more steepening and nonlinearity at the lower altitudes where dissipation is less efficient. As discussed in section 4.2, however, note that the continuum assumptions of Navier-Stokes equations are not violated even in the largest-amplitude case shown here ($Kn < 0.1$).

The neutral vertical velocities versus altitude and time are presented in Figure 9 to demonstrate the evolution of steep acoustic waves above the epicenter at different amplitudes. Note that in Figure 9a the amplitudes are such that the wave field appears nearly linear throughout the *F* region. Evidence of steepening in the wave field from ~200 to 350 km in Figure 9b after arrival of the waves demonstrates clearly the strength of the wave perturbations even for this weaker example case. As amplitudes increase further for the primary test case (2011 Tohoku) shown in Figure 9c, and for the doubled amplitude case in Figure 9d, the relative amplitudes of the second burst waves appears larger than the first as compared to previous cases. This is due to saturation of the wave field in the first arriving waves, where steepening is counteracted by dissipation,

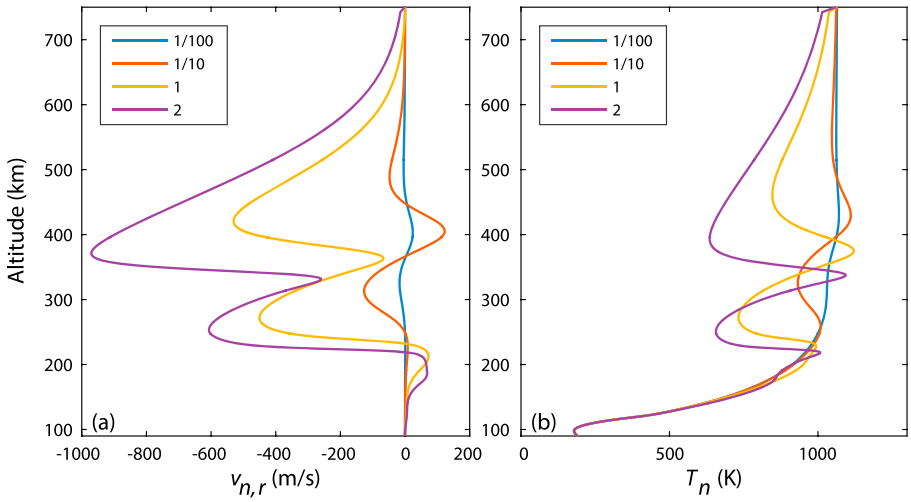

Figure 8. Thermospheric response to sources of different amplitudes (2× Tohoku, 1/10× Tohoku, and 1/100× Tohoku) for 6:03:22 UTC, i.e., same time as Figures 6g–6i. Each profiles is extracted form the centermost field line in the simulation. (a) Vertical component of the neutral velocity (positive downward along the field line in the Northern Hemisphere). (b) Neutral temperatures.

thus limiting the amplitude of the waves. This appears to be an important process in the observation; note that in Figure 2 the relative amplitudes of TEC perturbations due to the first and second bursts of waves are quite similar. Thus, it is reasonable to assume that viscous dissipation and nonlinearity limited the amplitude of the first arriving wave oscillations. The waves in our simulation thus "saturate" at a few hundred m/s

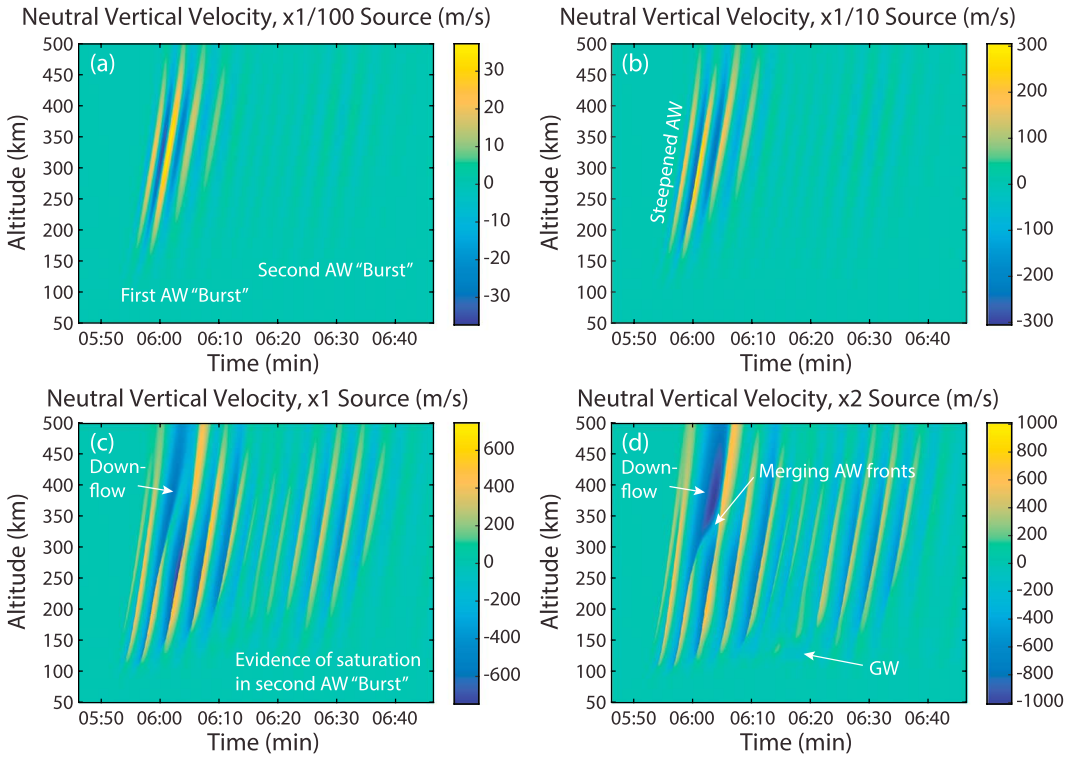

Figure 9. Epicentral neutral velocity evolutions over time for sources of different amplitudes, showing in Figures 9a–9d: Simulations with sources that are (a) 1/100×, (b) 1/10×, (c) equal, and (d) double to the estimated amplitude of the 2011 Tohoku earthquake sea surface responses, respectively. Acoustic wave (AW) and gravity wave (GW) activities are marked in each panel.

(when subtracting out the background flow created by the nonlinear wave impacts) and produce TEC oscillation signatures that are consistent with the observed TEC oscillations during both initial and subsequent burst events, suggesting reasonable consistency despite finite resolution of the numerical models.

Note that the strong first-arriving acoustic wave fronts in the first burst at large amplitudes may experience less reflection than the subsequent (more linear) waves within the same apparent packet, such that the second burst packet appears more symmetric in amplitude over time. The second packet also is able to evolve into a more coherent and extended wave train due to dispersion and partial reflections that would eventually lead to a persistent resonance. The two-way sound travel time between the ground and thermospheric temperature gradient is about 14–16 min for the conditions at the beginning of our simulation, which, very roughly, matches the time interval between the two bursts of acoustic activity. The nonlinearity of the waves, including the large background variations that they produce (e.g., Figure 6), prevents more accurate and simple descriptions of the reflection timing. In addition, partial reflections of the acoustic waves, which would be gradual process in the atmosphere, likely occur off of the both tropopause and the base of the thermosphere. Despite these complications, we do note the consistency of the modeled acoustic bursts with the data in terms of the TEC signatures shown in Figure 2.

A remarkable feature in Figure 9c, and especially Figure 9d, is the apparent merging and overtaking of the first arriving acoustic fronts into a longer period shock wave ~350 km altitude ~ 15 min after the event. This process was discussed first in section 4.2 and may explain the two-step formation of the depletion; it also acts to enhance the downward transport, by slowing the subsequently arriving fronts so that they dissipate effectively in place. As seen in Figure 9d, it also results in effectively longer period dynamics at altitudes near and above the *F* layer peak. It is reasonable to speculate that these dynamics may couple into longer period atmospheric motions, including evanescent acoustic gravity waves or thermospheric acoustic waves that cannot exist at altitudes below (enabled by the relatively longer cutoff period at thermospheric altitudes). Nonlinear acoustic wave processes such as observed here — shock merging and overtaking, wave frequency and mode conversion, and acoustic saturation — are appreciated in the context of stellar atmospheres [*Fleck and Schmitz*, 1993] and in the lower atmosphere following sonic booms during supersonic flight [*Gardner and Rogers*, 1979]. However, the occurrence of these processes at large scales in the thermosphere above a natural hazard event is remarkable and further underscores the difficulties in interpreting data sets for large-amplitude events.

6. Discussion and Conclusions

A detailed study of the impact of ocean uplifting sources of various amplitudes has been conducted with the atmospheric and ionospheric models described in *Zettergren and Snively* [2015]. A case study of the 2011 Tohoku earthquake is constructed by using a source of acoustic waves consistent with published accounts of the initial ocean surface response to the undersea earthquake. Results for modeled TEC indicate the formation of a vertical TEC depletion (~ −4 to −5 TECU) just south of the epicenter, following initial enhancements as the acoustic waves first impact the ionosphere. The basic features of the modeled depletions match observational results from *Saito et al.* [2011], *Kakinami et al.* [2012], and *Astafyeva et al.* [2013a] and are consistent with our reanalysis of absolute TEC values presented in Figure 2b. Modeled thermospheric responses to this "calibrated" run indicate very large wave amplitudes, with compressional velocities of ~250–300 m/s and superposed downward flows of ~300 m/s following dissipation and temperature variations of ~250–300 K. The relatively similar amplitudes of the first and second bursts of acoustic waves also support this theory, indicating that the first arriving wave burst was likely propagating in a saturated state, where nonlinearity and subsequent dissipation dominated its evolution and limited its amplitude. The arrival times of these bursts and the amplitudes of the embedded acoustic oscillations are also consistent with GPS TEC observations.

Similar to *Shinagawa et al.* [2013] and *Astafyeva et al.* [2013a] we attribute the formation of the ionospheric TEC depletion to the presence of nonlinear acoustic waves and their impacts. Additionally, our simulations and analyses have elucidated the detailed chain of processes leading to the TEC depletions for a wave spectrum that is consistent with *F* region GPS TEC observations. The initial, steep acoustic wave results in net upward transport in the thermosphere. This uplifted gas eventually begins to fall, thus causing the incoming acoustic wave fronts to slow as they propagate upward (since they are propagating in a falling background medium). As a result, these incoming wave fronts then dissipate more within the *F* region. For waves at large amplitudes, the slowed incoming wave fronts then may partly or fully merge with the next set of wave fronts that follow. The net impact of these nonlinear and dissipative processes is a mostly downward flow of the atmosphere

(and downward field-aligned ionospheric flow) around the time when the depletion is observed to form. This results in enhanced ionospheric recombination and strong northward transport of plasma leading to a TEC depletion that persists longer than the associated thermospheric dynamics.

Three additional model runs, showing the effects of varying source amplitude, indicate that only sources similar to that in our Tohoku reference case study are capable of inducing the semipermanent ionospheric responses (e.g., the TEC depletion). TEC and thermospheric responses for the smaller sources used in this study (1/100 × Tohoku and 1/10 × Tohoku) yield notably more linear responses (no large, semipermanent TEC depletions and only mild steepening of acoustic waves) as seen in Figure 7. All of the model runs indicate the presence of 3–4 min infrasonic fluctuations in TEC, which are subject to partial reflection and show clear evidence for the onset of acoustic resonance leading to persistence of these periodicities [e.g., *Saito et al.*, 2011]. Consistent with the results of *Zettergren and Snively* [2015], larger TEC perturbations are found to the magnetic south of the epicenter. Simultaneously generated gravity waves [e.g., *Matsumura et al.*, 2011] are also apparent in both the model simulations and TEC data, at similar scales, but with some evidence of meridional winds not captured by the present simulations. The relative amplitude of these longer period features—both primary gravity waves generated by the source and secondary wave-like features due to nonlinearity and dissipation in the acoustic wave field—increase with source amplitude clearly in contrast to the acoustic oscillation amplitude, which achieves saturation for the largest amplitude case studies presented.

Results presented here support the existence of strongly nonlinear large-amplitude acoustic waves in the thermosphere-ionosphere system following strong sea surface forcing. In particular, the amplitude and persistent character of the observed and modeled TEC perturbations imply that thermospheric acoustic waves with saturated compressional velocities up to ~300 m/s may exist following the largest undersea earthquake events. Weaker model sources are insufficient to produce the strong and nonlinear ionospheric responses necessary to form the semipermanent TEC depletions identified in the observations. Hence, these large infrasonic wave amplitudes in our model results are *required* to explain the range of effects observed during the 2011 Tohoku event. More generally, this work has quantitatively illustrated the parameter space of TEC, ionospheric, and thermospheric responses to be expected from vertical disturbances by undersea earthquakes of varying amplitudes.

This reported mechanism, while apparently robust under average conditions, does depend on multiple parameters, and its complex sensitivity to these remains to be fully investigated in general. These include the 3-D directivity of the acoustic wave field, the exact amplitude, duration, and spectrum of the source, and the ambient states of the thermosphere and ionosphere as they vary, e.g., with geographic location, solar and geomagnetic activity, and local time. The ionospheric recovery timescales following the formation of the depletion will also depend on the ambient state parameters in addition to the specific neutral wave dynamics. In order to more accurately estimate both the TEC and magnetic fluctuations resulting from earthquakes, comprehensive 3-D models and case studies will be developed to address the remaining simplifications of these and related prior studies [*Zettergren and Snively*, 2013, 2015]. Indeed, we believe that the omission of the third dimension for both the atmosphere and ionosphere, which here precludes specification of a fully realistic simulated ocean surface response and atmospheric winds, can plausibly explain many of the remaining discrepancies between model simulations and observed data. Future 3-D modeling, spanning from ocean surface source to subsequent atmospheric wave propagation and resulting ionospheric responses, will naturally lead to improved model reconstructions of event scenarios and observable signatures.

Acknowledgments
Research was supported by NASA grant NNX14AQ39G to Embry-Riddle Aeronautical University. Models used in this study were developed under support from NSF CAREER grants AGS-1255181 and AGS-1151746. Portions of this work were done at the Jet Propulsion Laboratory, California Institute of Technology, under a contract with the National Aeronautics and Space Administration. Data used to generate plots are available upon request to the authors.

References

Arai, N., M. Iwakuni, S. Watada, Y. Imanishi, T. Murayama, and M. Nogami (2011), Atmospheric boundary waves excited by the tsunami generation related to the 2011 great Tohoku-oki earthquake, *Geophys. Res. Lett.*, *38*, L00G18, doi:10.1029/2011GL49146.

Artru, J., V. Ducic, H. Kanamori, P. Lognonné, and M. Murakami (2005), Ionospheric detection of gravity waves induced by tsunamis, *Geophys. J. Int.*, *160*(3), 840–848.

Astafyeva, E., S. Shalimov, E. Olshanskaya, and P. Lognonné (2013a), Ionospheric response to earthquakes of different magnitudes: Larger quakes perturb the ionosphere stronger and longer, *Geophys. Res. Lett.*, *40*, 1675–1681, doi:10.1002/grl.50398.

Astafyeva, E., L. Rolland, P. Lognonné, K. Khelfi, and T. Yahagi (2013b), Parameters of seismic source as deduced from 1 Hz ionospheric GPS data: Case study of the 2011 Tohoku-oki event, *J. Geophys. Res. Space Physics*, *118*, 5942–5950, doi:10.1002/jgra.50556.

Bale, D. S., R. J. LeVeque, S. Mitran, and J. A. Rossmanith (2002), A wave propagation method for conservation laws and balance laws with spatially-varying flux functions, *SIAM J. Sci. Comput.*, *24*, 955–978.

Broutman, D., S. D. Eckermann, and D. P. Drob (2014), The partial reflection of tsunami-generated gravity waves, *J. Atmos. Sci.*, *71*(9), 3416–3426.

Brown, S. L. (1996), Approximate Riemann solvers for moment models of dilute gases, PhD thesis, Univ. of Michigan.

Fleck, B., and F. Schmitz (1993), On the interactions of hydrodynamic shock waves in stellar atmospheres, *Astron. Astrophys.*, *273*, 671–683.

Galvan, D. A., A. Komjathy, M. P. Hickey, P. Stephens, J. B. Snively, Y. T. Song, M. D. Butala, and A. J. Mannucci (2012), Ionospheric signatures of Tohoku-Oki tsunami of March 11, 2011: Model comparisons near the epicenter, *Radio Science*, *47*, RS4003, doi:10.1029/2012RS005023.

Garcia, R. F., S. Bruinsma, P. Lognonné, E. Doornbos, and F. Cachoux (2013), GOCE: The first seismometer in orbit around the Earth, *Geophys. Res. Lett.*, *40*, 1015–1020, doi:10.1002/grl.50205.

Gardner, J. H., and P. H. Rogers (1979), Thermospheric propagation of sonic booms from the Concorde supersonic transport, NRL Memorandum Rep. 3904.

Garriott, O. K. (1969), *Introduction to Ionospheric Physics*, Academic Press, New York.

Hao, Y., Z. Xiao, and D. Zhang (2012), Multi-instrument observation on co-seismic ionospheric effects after Great Tohoku earthquake, *J. Geophys. Res.*, *117*, A02305, doi:10.1029/2011JA017036.

Hao, Y., Z. Xiao, and D. Zhang (2013), Teleseismic Magnetic Effects (TMDS) of 2011 Tohoku earthquake, *J. Geophys. Res. Space Physics*, *118*, 3914–3923, doi:10.1002/jgra.50326.

Hickey, M., G. Schubert, and R. Walterscheid (2009), Propagation of tsunami-driven gravity waves into the thermosphere and ionosphere, *J. Geophys. Res.*, *114*, A08304, doi:10.1029/2009JA014105.

Hines, C. O. (1960), Internal atmospheric gravity waves at ionospheric heights, *Can. J. Phys.*, *38*, 1441–1481.

Huba, J., D. Drob, T.-W. Wu, and J. Makela (2015), Modeling the ionospheric impact of tsunami-driven gravity waves with SAMI3: Conjugate effects, *Geophys. Res. Lett.*, *42*, 5719–5726, doi:10.1002/2015GL064871.

Huba, J. D., G. Joyce, and J. A. Fedder (2000), Sami2 is Another Model of the Ionosphere (SAMI2): A new low-latitude ionosphere model, *J. Geophys. Res.*, *105*, 23,035–23,054, doi:10.1029/2000JA000035.

Kakinami, Y., M. Kamogawa, Y. Tanioka, S. Watanabe, A. R. Gusman, J.-Y. Liu, Y. Watanabe, and T. Mogi (2012), Tsunamigenic ionospheric hole, *Geophys. Res. Lett.*, *39*, L00G27, doi:10.1029/2011GL050159.

Kamogawa, M., T. Kanaya, Y. Orihara, A. Toyoda, Y. Suzuki, S. Togo, and J.-Y. Liu (2015), Does an ionospheric hole appear after an inland earthquake?, *J. Geophys. Res. Space Physics*, *120*, 9998–10,005, doi:10.1002/2015JA021476.

Komjathy, A., D. A. Galvan, P. Stephens, M. Butala, V. Akopian, B. Wilson, O. Verkhoglyadova, A. J. Mannucci, and M. Hickey (2012), Detecting ionospheric TEC perturbations caused by natural hazards using a global network of GPS receivers: The Tohoku case study, *Earth Planet. Space*, *64*(12), 1287–1294.

LeVeque, R. J. (2002), *Finite Volume Methods for Hyperbolic Problems*, Cambridge Univ. Press.

Maeda, T., T. Furumura, S. Sakai, and M. Shinohara (2011), Significant tsunami observed at ocean-bottom pressure gauges during the 2011 off the Pacific coast of Tohoku earthquake, *Earth Planets Space*, *63*(7), 803–808.

Maruyama, T., and H. Shinagawa (2014), Infrasonic sounds excited by seismic waves of the 2011 Tohoku-oki earthquake as visualized in ionograms, *J. Geophys. Res. Space Physics*, *119*, 4094–4108, doi:10.1002/2013JA019707.

Maruyama, T., T. Tsugawa, H. Kato, A. Saito, Y. Otsuka, and M. Nishioka (2011), Ionospheric multiple stratifications and irregularities induced by the 2011 off the Pacific coast of Tohoku earthquake, *Earth Planets Space*, *63*(7), 869–873.

Matsumura, M., A. Saito, T. Iyemori, H. Shinagawa, T. Tsugawa, Y. Otsuka, M. Nishioka, and C. H. Chen (2011), Numerical simulations of atmospheric waves excited by the 2011 off the Pacific coast of Tohoku earthquake, *Earth Planets Space*, *63*(7), 885–889, doi:10.5047/eps.2011.07.015.

Mikumo, T., M. Garces, T. Shibutani, W. Morii, T. Okawa, and Y. Ishihara (2013), Acoustic-gravity waves from the source region of the 2011 Great Tohoku earthquake ($M_w = 9.0$), *J. Geophys. Res. Solid Earth*, *118*, 1534–1545, doi:10.1002/jgrb.50143.

Occhipinti, G., P. Lognonné, E. A. Kherani, and H. Hébert (2006), Three-dimensional waveform modeling of ionospheric signature induced by the 2004 Sumatra tsunami, *Geophys. Res. Lett.*, *33*, L20104, doi:10.1029/2006GL026865.

Perevalova, N., V. Sankov, E. Astafyeva, and D. Zhupityaeva (2014), Threshold magnitude for ionospheric TEC response to earthquakes, *J. Atmos. Sol. Terr. Phys.*, *108*, 77–90.

Rolland, L., G. Occhipinti, P. Lognonné, and A. Loevenbruck (2010), The 29 september 2009 Samoan tsunami in the ionosphere detected offshore Hawaii, *Geophys. Res. Lett.*, *37*, L17191, doi:10.1029/2010GL044479.

Rolland, L. M., P. Lognonné, and H. Munekane (2011), Detection and modeling of rayleigh wave induced patterns in the ionosphere, *J. Geophys. Res.*, *116*, A05320, doi:10.1029/2010JA016060.

Saito, A., T. Tsugawa, Y. Otsuka, M. Nishioka, T. Iyemori, M. Matsumura, S. Saito, C. H. Chen, Y. Goi, and N. Choosakul (2011), Acoustic resonance and plasma depletion detected by GPS total electron content observations after the 2011 off the Pacific coast of Tohoku earthquake, *Earth Planets Space*, *63*, 863–867, doi:10.5047/eps.2011.06.034.

Shinagawa, H., T. Iyemori, S. Saito, and T. Maruyama (2007), A numerical simulation of ionospheric and atmospheric variations associated with the Sumatra earthquake on December 26, 2004, *Earth Planets Space*, *59*(9), 1015–1026.

Shinagawa, H., T. Tsugawa, M. Matsumura, T. Iyemori, A. Saito, T. Maruyama, H. Jin, M. Nishioka, and Y. Otsuka (2013), Two-dimensional simulation of ionospheric variations in the vicinity of the epicenter of the Tohoku-Oki earthquake on 11 March 2011, *Geophys. Res. Lett.*, *40*, 5009–5013, doi:10.1002/2013GL057627.

Snively, J. B. (2013), Mesospheric hydroxyl airglow signatures of acoustic and gravity waves generated by transient tropospheric forcing, *Geophys. Res. Lett.*, *40*, 4533–4537, doi:10.1002/grl.50886.

Snively, J. B., and V. P. Pasko (2008), Excitation of ducted gravity waves in the lower thermosphere by tropospheric sources, *J. Geophys. Res.*, *113*(A06303), doi:10.1029/2007JA012693.

Tsugawa, T., A. Saito, Y. Otsuka, M. Nishioka, T. Maruyama, H. Kato, T. Nagatsuma, and K. T. Murata (2011), Ionospheric disturbances detected by GPS total electron content observation after the 2011 off the Pacific coast of Tohoku earthquake, *Earth Planets Space*, *63*, 875–879, doi:10.5047/eps.2011.06.035.

Tsushima, H., K. Hirata, Y. Hayashi, Y. Tanioka, K. Kimura, S. Sakai, M. Shinohara, T. Kanazawa, R. Hino, and K. Maeda (2011), Near-field tsunami forecasting using offshore tsunami data from the 2011 off the Pacific coast of Tohoku earthquake, *Earth Planets Space*, *63*(7), 821–826.

Utada, H., H. Shimizu, T. Ogawa, T. Maeda, T. Furumura, T. Yamamoto, N. Yamazaki, Y. Yoshitake, and S. Nagamachi (2011), Geomagnetic field changes in response to the 2011 off the Pacific coast of Tohoku earthquake and tsunami, *Earth Planet. Sci. Lett.*, *311*(1), 11–27.

Vadas, S. L., J. J. Makela, M. J. Nicolls, and R. F. Milliff (2015), Excitation of gravity waves by ocean surface wave packets: Upward propagation and reconstruction of the thermospheric gravity wave field, *J. Geophys. Res. Space Physics*, *120*, 9748–9780, doi:10.1002/2015JA021430.

Wei, C., O. Bühler, and E. G. Tabak (2015), Evolution of tsunami-induced internal acoustic-gravity waves, *J. Atmos. Sci.*, *72*, 2303–2317.

Yang, Y.-M., X. Meng, A. Komjathy, O. Verkholyadova, R. Langley, B. Tsurutani, and A. Mannucci (2014), Tohoku-oki earthquake caused major ionospheric disturbances at 450 km altitude over Alaska, *Radio Sci.*, *49*, 1206–1213, doi:10.1002/2014RS005580.

Zettergren, M., and J. Snively (2015), Ionospheric response to infrasonic-acoustic waves generated by natural hazard events, *J. Geophys. Res. Space Physics*, *120*, 8002–8024.

Zettergren, M. D., and J. Semeter (2012), Ionospheric plasma transport and loss in auroral downward current regions, *J. Geophys. Res.*, *117*, A06306, doi:10.1029/2012JA017637.

Zettergren, M. D., and J. B. Snively (2013), Ionospheric signatures of acoustic waves generated by transient tropospheric forcing, *Geophys. Res. Lett.*, *40*, 5345–5349, doi:10.1002/2013GL058018.